ADVANCED OPTICAL MATERIALS
www.advopticalmat.de

Vacuum-Deposited Perovskite Photodiodes for Visible and X-Ray Photon Detection

Lucía Martínez-Goyeneche, Riccardo Ollearo, Camilla Bordoni, Andrea Ciavatti, Albert J. J. M. van Breemen, Gerwin H. Gelinck, Beatrice Fraboni, Daniel Tordera, and Michele Sessolo**

Metal halide perovskite photodiodes have garnered extensive attention owing to their favorable optoelectronic properties, rendering them attractive for visible, near-infrared, and X-ray sensors. However, their predominant reliance on solution-processing deposition techniques poses challenges for seamless integration into existing industrial processes. In this study, this limitation is addressed by developing fully vacuum-processed perovskite photodiodes with varying hole transport layers (HTL). These findings underscore the critical role of HTL selection in influencing the dark and noise current characteristics of the diodes. With an optimized HTL, photodiodes are obtained with low noise current (≈3 10^{-14} A $Hz^{-1/2}$) and high specific detectivity (≈10^{12} Jones at 710 nm at −0.5 V). The photodiodes are also tested as X-ray detectors and are found to be stable under X-ray radiation, with state-of-the-art sensitivity of 33 ± 4 µC Gy^{-1} cm^{-2} and a low limit of detection of 2.0 ± 1.6 µG s^{-1}. These insights contribute to the development of perovskite photodiodes with improved performance and broader industrial applicability.

1. Introduction

Metal halide perovskites are one of the most promising materials for future optoelectronic applications such as photovoltaic cells or light-emitting diodes.[1,2] These materials can be described by their distinctive chemical structure ABX_3, where A is a monovalent cation (often organic), B is a divalent metal and X is a halide.[3] In particular, perovskites incorporating Pb^{2+} in the divalent site have shown superior semiconducting properties, such as long charge diffusion length, ambipolar carrier mobility, high optical absorption coefficient, as well as bandgap tunability by changing the X halide and monovalent A cation.[4–7] The recent successful implementation in solar cells using perovskites as active materials, with efficiencies reaching 26%,[8] have encouraged the study of sister optoelectronic devices such as photodetectors. Photodetectors also convert the impinging light into electronic signals but are commonly operated at negative bias to maximize current collection. They are used in a wide range of applications such as imaging, optical communications, gesture recognition or biomedical sensing, amongst others.[9–13]

Perovskite-based photodetector technologies, and in particular photodiodes, are rapidly closing the gap with their inorganic counterparts in terms of device performance, such as dark current (J_d), external quantum efficiency (EQE) and specific detectivity (D^*).[14,15] Specifically, D^* up to 10^{13} Jones have been demonstrated in the visible range,[15,16] values in line with other technologies such as organic semiconductors, and approaching that of commercial Si.[17,18] It comes to no surprise that perovskite photodetectors have garnered interest as they combine the desirable optoelectronic properties of perovskites with the advantages of thin-film devices, such as transparency, flexibility and ease of integration.[19,20] As a result, perovskite photodetectors for visible, near infrared and X-ray photons have been demonstrated.[20–25]

Most of the reported perovskite photodetectors are prepared by solution-processing methods. These processes are convenient on a lab scale, but are not readily transferable to industry, as they are often restricted to small area and use steps that are challenging to scale up, such as anti-solvent processing.[26] On the other hand, vacuum deposition does not require the use of a solvent, is a low-temperature technique, allows for miniaturization and, more importantly, is already implemented in the

L. Martínez-Goyeneche, D. Tordera, M. Sessolo
Instituto de Ciencia Molecular
Universidad de Valencia
C/ Catedrático J. Beltrán 2, Paterna 46980, Spain
E-mail: daniel.tordera@uv.es; michele.sessolo@uv.es
R. Ollearo, A. J. J. M. van Breemen, G. H. Gelinck
TNO at Holst Centre
High Tech Campus 31, Eindhoven 5656 AE, The Netherlands
C. Bordoni, A. Ciavatti, B. Fraboni
Department of Physics and Astronomy
Alma Mater Studiorum – University of Bologna
Viale C. Berti-Pichat 6/2, Bologna 40127, Italy

The ORCID identification number(s) for the author(s) of this article can be found under https://doi.org/10.1002/adom.202400464

DOI: 10.1002/adom.202400464

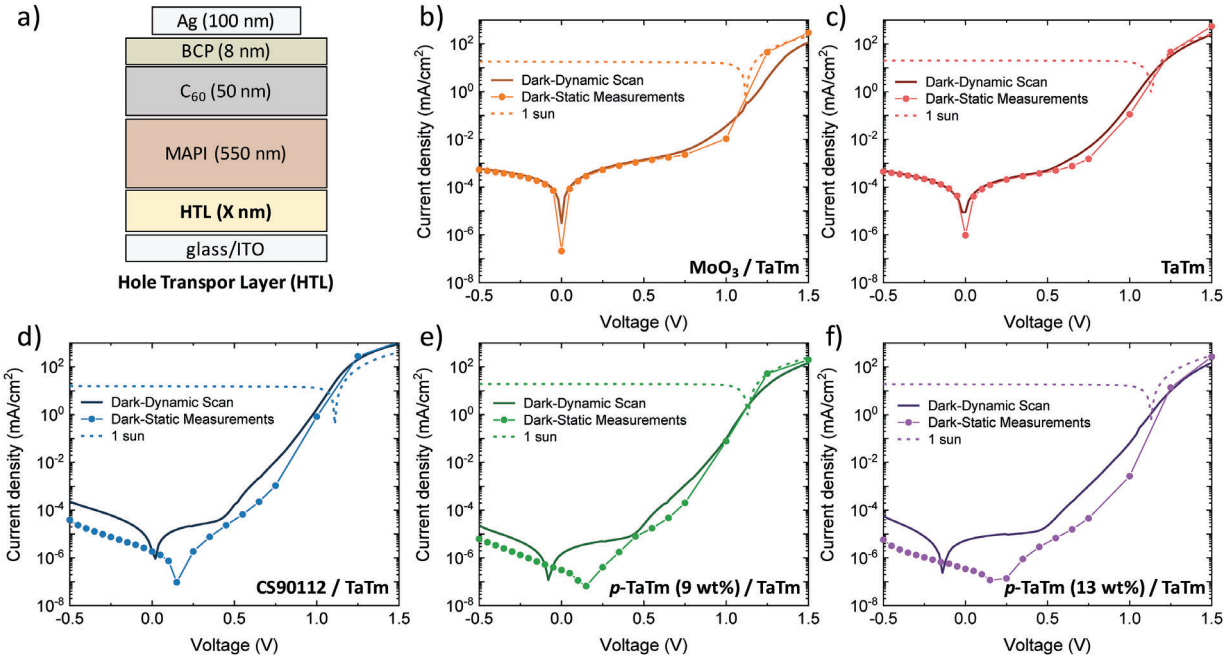

Figure 1. a) Schematic device structure of the vacuum deposited perovskite photodiodes. *J–V* characteristics in dark (dynamic scan: solid line, static scan: line and symbols) and under 100 mW cm^{-2} illumination (dashed line) for photodiodes with five different HTLs: b) MoO_3/TaTm, c) TaTm, d) CS90112/TaTm, e) TaTm:CS90112 (9 wt%)/TaTm, and f) TaTm:CS90112 (13 wt%)/TaTm.

industry.[27] Therefore, research on perovskite photodetectors using dry, vacuum-processing methods is of high interest. However, as for vacuum-processed perovskite solar cells, only a limited number of examples have been reported on vacuum-deposited perovskite photodetectors.[28–34] Another advantage of vacuum processing is the possibility to fabricate multilayer devices without concerns about damaging the underlying layers. Multilayers are used in state-of-the-art devices to maximize performance, as each layer is designed to carry out one specific process contributing to the device function.

Recently, it has been shown that the electron blocking layer (EBL, or hole transport layer, HTL), and more precisely the energy offset between the highest occupied molecular orbital (HOMO) of the HTL and the perovskite conduction band minimum, plays a key role in the determination of the dark current and noise, and hence the specific detectivity, of perovskite photodiodes.[35,36] However, other factors such as wetting, perovskite film formation, and crystallization due to the use of different bottom HTLs may also influence recombination at the HTL/perovskite interface, hence affecting the detector characteristics.

In this work, we have prepared fully vacuum-processed perovskite photodiodes using methyl ammonium lead iodide (MAPI) as the active material, with HTL combinations representative of most organic and perovskite optoelectronic devices. The work investigates the relation of the HTL with the performance of the devices, highlighting the importance of the HTL selection in order to fabricate efficient perovskite detectors. The photodiodes are characterized both in the visible and X-ray spectrum. In the visible range, devices show low dark currents, high EQE (up to 90% in the visible range), and detectivity close to 10^{13} Jones. The perovskite diodes are also used to detect X-ray radiation up to 150 kVp, obtaining a linear response in a wide range of X-ray irradiance, for both high and low X-ray doses, with a low limit of detection of 2.0 μG s^{-1}. The sensitivity is the highest reported so far for thin film X-ray perovskite photodiodes.

2. Results and Discussion

Perovskite photodiodes with five different HTLs were fabricated in a p-i-n configuration (**Figure 1**a). The diodes consist of MAPI perovskite films, the semiconductor responsible for the carrier generation, sandwiched between an electron transport layers (ETL, also acting as hole blocking layer) and an HTL, and eventual additional layers to ensure ohmic contact with the bottom ITO and top silver electrodes (flat band energy diagram in Figure S1, Supporting Information). The selected hole transport materials (**Table 1**) are commonly used in efficient, vacuum-deposited photovoltaic devices.[37–40]

The device stack is ITO/HTL/MAPI (550 nm)/C_{60} (50 nm)/BCP (8 nm)/Ag (where C_{60} is fullerene and BCP is bathocuproine). Thick C_{60} layers were intentionally used to achieve lower dark current values.[41] The investigated HTLs were chosen as the most representative for organic optoelectronic devices, and include thin organic semiconductors, the combination of a high-work function metal oxide and an organic semiconductor, a thin organic dopant layer coated with an intrinsic organic semiconductor, and a combination of doped and intrinsic organic semiconductors. The detailed structures are MoO_3 (5.5 nm)/TaTm (10 nm), TaTm (5 nm), CS90112 (2.5 nm)/TaTm (10 nm), TaTm:CS90112 (9 wt%, 20 nm)/TaTm (10 nm) and TaTm:CS90112 (13 wt%, 20 nm)/TaTm (10 nm), where TaTm is *N*4,*N*4,*N*4″,*N*4″-tetra([1,1′-biphenyl]−4-yl)-[1,1′:4′,1″-terphenyl]−4,4″-diamine, MoO_3 is molybdenum oxide and CS90112 is 2,2′,2″-(cyclopropane-1,2,3-triylidene)tris

Table 1. Overview of the device structures evaluated in this study, highlighting the different HTLs and eventual hole injection layers (HILs).

	HIL	HTL	
ITO	MoO_3 (5.5 nm)	TaTm (10 nm)	MAPI/C_{60} (50 nm)/BCP (8 nm)/Ag
	–	TaTm (5 nm)	
	CS90112 (2.5 nm)	TaTm (10 nm)	
	TaTm:CS90112 (9 wt%)	TaTm (10 nm)	
	TaTm:CS90112 (13 wt%)	TaTm (10 nm)	

(2-(p-cyanotetrafluorophenyl)acetonitrile). TaTm is an intrinsic organic semiconductor that acts as HTL (previously reported by us and others in perovskite solar cells and photodiodes),[30] while MoO_3 and CS90112 are used to improve the carrier extraction to the transparent bottom electrode in the p-i-n configuration.[42–44] The notation TaTm:CS90112 indicates that the two materials are co-sublimed (with CS90112 at 9 and 13 wt% as indicated) in order to increase the conductivity of the film used as the hole injection layer.[45] All layers are deposited by thermal vacuum deposition. Fabrication details are described in the experimental section.[45,46]

Current density versus voltage (*J*–*V*) characteristics of the photodiodes were obtained in dark and under a 100 mW cm^{-2} (1 Sun) illumination (dashed line) (Figure 1b–f). The main key parameters to evaluate the performance of the perovskite photodiodes are summarized in **Table 2**. *J*–*V* characteristics in dark were recorded dynamically (solid line) and statically (line and circles). Dynamic scans consisted in a voltage scan from −0.5 to 1.5 V with a rate of 0.05 V s^{-1}, while in static measurements a constant voltage was maintained, and the dark current was measured as a function of time at different voltage points (Figure S2, Supporting Information). This is considered a more reliable way to determine the dark current, as photodiodes are generally driven in reverse and constant applied bias.[15,35,47] All devices show a similar photocurrent value of approximately 18 mA cm^{-2} at −0.5 V. Regarding the dark current, photodiodes with MoO_3/TaTm and TaTm as HTLs (Figure 1b,c), exhibit similar values, ≈5 10^{-4} mA cm^{-2} at −0.5 V, and static and dynamic dark curves can be superimposed. This might originate from the relatively high (ohmic) leakage current observed for these HTLs, as observable from the symmetric linear regime around short circuit. On the other hand, devices incorporating CS90112 and TaTm (Figure 1d–f) exhibit much lower dark current, with values of $4{\cdot}10^{-5}$ mA cm^{-2} at −0.5 V for CS90112/TaTm and ≈$6{\cdot}10^{-6}$ mA cm^{-2} when the HTL is TaTm:CS90112/TaTm. Static measurements are almost one order of magnitude lower than dynamic scans, because at these low dark current values, transient currents play a significant role. Photovoltaic parameters of the perovskite diodes were also estimated and are summarized in Table S1 (Supporting Information), showing values in line with vacuum-processed perovskite solar cells with similar device structure.[40,42,43]

Figure 2a illustrates the EQE spectra of the different photodiodes. In all cases, a broadband response is observed in the full visible spectrum, with average values over 80% and maximum values up to 90% in the green region (500 – 550 nm). The minimum observed for all devices at ≈650 nm is due to optical interference.[48] The EQE is independent of the applied bias voltage (see EQE at 0 V, Figure S3, Supporting Information), as previously reported.[34] Photodiodes incorporating the 5 nm thick TaTm display an enhanced spectral response in the ultraviolet (UV) region of the electromagnetic spectrum (350–420 nm). Using a thicker TaTm layer results in a higher parasitic absorption in the UV region, hence a lower EQE and short-circuit current density, J_{sc} (Table S1, Supporting Information). The specific detectivity (D^*) is a key figure of merit used to quantify the weakest detectable light signal. In reverse bias the formula of the specific detectivity can be simplified under the assumption of a predominating shot noise as:

$$D^* = R/\sqrt{2eJ_{dark}} \quad (1)$$

where *e* is the elementary charge and R is the responsivity (Figure S4a, Supporting Information). The measured low dark current and high EQE result in high shot-noise D^* (Figure 2b). As the responsivity is similar for all photodiodes, the shot-noise detectivity follows an inverse trend to that of the dark current, reaching values of $1.1{\cdot}10^{13}$ Jones at 710 nm under a bias of −0.5 V for both photodiodes using TaTm:CS90112/TaTm as HTL.

Table 2. Photodiode figures of merit incorporating the different hole transport layers and measured at −0.5 reverse bias if not otherwise stated.

HTL	J_{dark} [mA cm^{-2}][a)]	R_{max} [A/W]	Shot-noise D^*_{max} [Jones]	i_{noise} [A/$Hz^{1/2}$]	D^*_{max} [Jones]
MoO_3/TaTm	$5.3{\cdot}10^{-4}$	0.46	$1.1{\cdot}10^{12}$	$1.3{\cdot}10^{-13}$	$3.6{\cdot}10^{11}$
TaTm	$4.5{\cdot}10^{-4}$	0.48	$1.3{\cdot}10^{12}$	$1.2{\cdot}10^{-13}$	$4.0{\cdot}10^{11}$
CS90112/TaTm	$3.9{\cdot}10^{-5}$	0.47	$4.2{\cdot}10^{12}$	$5.7{\cdot}10^{-14}$	$8.3{\cdot}10^{11}$
TaTm:CS90112 (9 wt%)/TaTm	$6.3{\cdot}10^{-6}$	0.48	$1.1{\cdot}10^{13}$	$3.8{\cdot}10^{-14}$	$1.3{\cdot}10^{12}$
TaTm:CS90112 (13 wt%)/TaTm	$5.7{\cdot}10^{-6}$	0.46	$1.1{\cdot}10^{13}$	$3.5{\cdot}10^{-14}$	$1.3{\cdot}10^{12}$

[a)] Static measurement of the dark current (Figure S4b, Supporting Information).

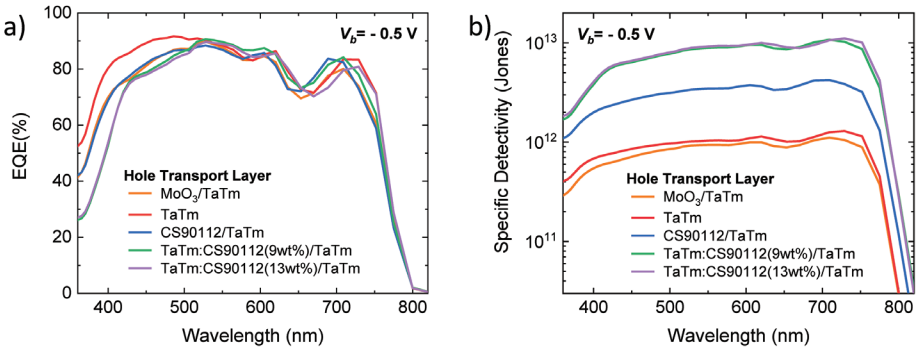

Figure 2. a) External quantum efficiency (EQE) as a function of photon wavelength recorded at a reverse bias of −0.5 V and b) Shot-noise specific detectivity as a function of wavelength at −0.5 V.

Although specific detectivity has been commonly reported in literature under the assumption of a predominating shot noise,[28,49–53] this approximation results in an overestimation of D^*, as other sources of noise are non-negligible.[35] Moreover, another often-used assumption is to consider the noise to be "white", i.e., frequency independent.[54] However, there may be contributions to the noise current that are frequency dependent, such as flicker or pink noise ($1/f$), and elements of static and dynamic disorder (generally originated from carrier trapping/detrapping processes).[55] Hence, a more rigorous definition of the specific detectivity is defined as:

$$D^* = \frac{R\sqrt{A \cdot \Delta f}}{i_{noise}} \quad (2)$$

where i_{noise} is the noise current, A is the active area and Δf is the electrical bandwidth. In order to precisely determine the specific detectivity of our devices, we characterized the noise current versus frequency at −0.5 V in the frequency interval from 1 to 100 Hz (**Figure 3a**). In all cases, the spectra are almost frequency independent, indicating that the $1/f$ component is negligible, and hence the noise of the photodiodes is dominated by white noise. Following the trend of dark current, photodiodes including bilayer HTLs based on TaTm and CS90112 exhibit lower noise current, achieving an average noise level of ≈40 fA Hz^{-1} at −0.5 V for the photodiodes using TaTm:CS90112/TaTm as the HTL. The noise is also independent of the applied bias voltage (see noise current versus frequency at 0 V, Figure S5 (Supporting Information) and calculated noise equivalent power in Figure S6, Supporting Information). Clearly, when taking into account other sources of noise, the obtained specific detectivity is nearly one

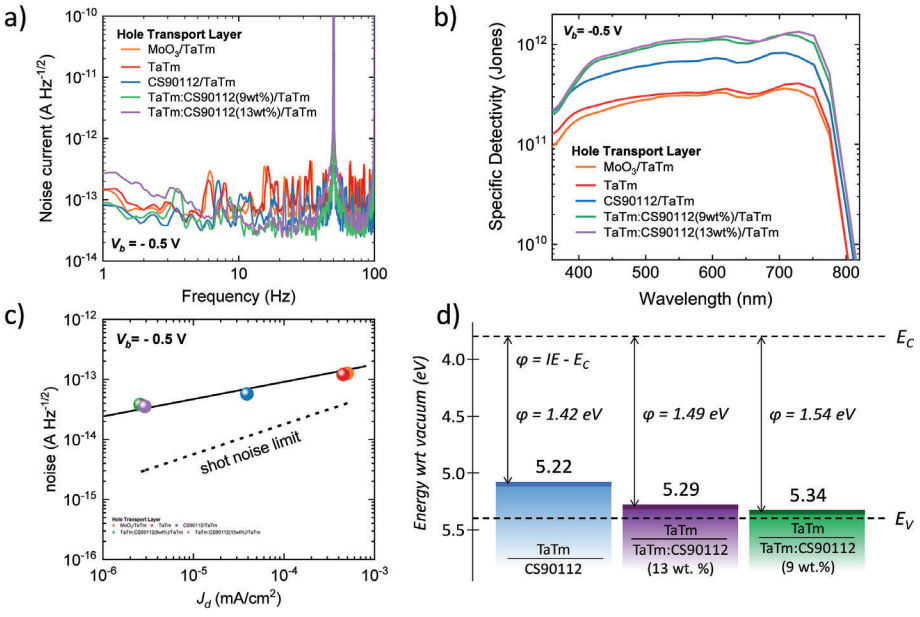

Figure 3. a) Noise current versus frequency (1-100 Hz) measured at −0.5 V. b) Specific detectivity under reverse bias of −0.5 V calculated using the measured noise current. c) Average noise current versus dark current density at −0.5 V for the different photodiodes. Colored circles indicate average noise values extrapolated from the frequency region between 1–100 Hz. The shot noise limit is also plotted for comparison (dashed line). d) Schematic of the ionization energy (IE) of the HTLs incorporating TaTm and CS90112 obtained by UPS, with respect to the perovskite conduction and valence band (E_C and E_V, respectively, values from literature).[58] The energy barrier between the HTL IE and the perovskite E_C is also highlighted.

order of magnitude lower than the shot-noise detectivity. This is shown in Figure 3b where the specific detectivity is calculated using Equation (2) with measured values of the noise current (averaged between 1 and 100 Hz). In this case, the photodiodes including TaTm:CS90112/TaTm as the HTL show a specific detectivity of $\approx 1.3 \cdot 10^{12}$ at 710 nm, under a bias of −0.5 V. These values are similar to previously reported specific detectivity for perovskite photodiodes under the same bias conditions and considering the noise current (Table S2, Supporting Information).[35,41,56] The same device shows a linear dynamic range (LDR) of 126 dB (Figure S7, Supporting Information). The relation between the average noise current and the dark current density of the photodiodes is shown in Figure 3c. The shot noise is also plotted for reference (dashed line), and is calculated from the dark current according to the following expression:

$$i_{n,\ shot} = \sqrt{2eBI_{dark}} \tag{3}$$

where B is the electrical bandwidth. The average experimental noise current is one order of magnitude higher than the shot noise, showing the importance to determine the specific detectivity taking into account all possible sources of noise.[30,35,57] Recently, it was demonstrated that thermal generation at the HTL/perovskite interface is the primary source of dark current in solution-processed perovskite photodiodes.[35] In particular, the activation energy of the dark current is correlated with the energy difference (φ) between the HOMO of the HTL and the conduction band minimum (E_C) of the perovskite, where thermal charge generation can occur.

In order to assess if a similar mechanism might explain the trends observed in our vacuum-deposited photodiodes, we measured the ionization energy (IE) of the HTLs with lower J_D (those combining TaTm and CS90112) by ultraviolet photoemission spectroscopy (UPS, Figure S8, Supporting Information). The IE is an experimentally accessible approximation of the HOMO level of a material in the solid state. A schematic flat band energy diagram of the MAPI interface with the three different HTLs is shown in Figure 3d. Indeed, when the energy difference φ increases, J_D was found to decrease accordingly (Figure S9, Supporting Information), which is in agreement with the role of thermal generation at this interface. Hence, in general, HTLs with high IE (HOMO) are preferred, as long as the IE is not higher than the perovskite valence band maximum (E_V), which would result in unfavorable charge extraction and recombination, as previously reported.[39]

In summary, devices using TaTm:CS90112 (9 wt%, 20 nm)/TaTm(10 nm) as the HTL show the highest specific detectivity in the visible spectrum, consequence of the low dark and noise currents. Hence, we selected this device stack to be assessed as an X-ray detector. It is known that thin films absorb only a small fraction of high-energy X-ray photons due to the small absorbing material thickness.[59,60] On the other hand, when the active layer is thick, it is susceptible to radiation damage, and high-voltage operation is necessary for efficient charge collection.[61] We fabricated devices with both 550 and 1000 nm thick perovskite films (cross section SEM in Figure S10, Supporting Information). **Figure** 4a,b shows the photocurrent of devices under different incident dose rates of X-ray irradiation (1482, 3237, 4911, 6667, and 8354 μGy s^{-1}) with a 20 s modulation period of the X-ray beam. The characterization of the devices was carried out at 0 V to maximize the signal-to-noise ratio. Thicker perovskite (1 μm) devices show slower time response to X-ray (Figure 4b), likely a consequence of the longer charge drifting time. After X-ray irradiation, the dark current of both devices shows values comparable to pre-irradiation ones, indicating that the photodiodes are X-ray radiation-tolerant (Figure S11, Supporting Information). Figure 4c illustrates the linear response of the extracted photocurrent as a function of the dose rates (from 1482 to 8354 μGy s^{-1}), and the respective linear fit. In general, high values of collected photocurrent as a function of dose rates indicate a high sensitivity, an important figure of merit used to validate X-ray detectors performance. The sensitivity is the slope of the linear fit, normalized by the device effective area, equal to 7.8 ± 0.6 and 33 ± 4 μC Gy^{-1} cm^{-2} for 550 nm and 1 μm thick perovskite films, respectively. The values are the average over 8 devices for each thickness, therefore, the low associated error indicates the good reproducibility of the deposition process. Photodiodes based on thicker perovskite films show higher X-ray sensitivity due to the higher photon absorption, hence increased photocurrent. The sensitivity of 550 nm thick devices is comparable to those reported for thin film perovskite X-ray detectors with similar thicknesses under a short-circuit operation mode.[62–64] To the best of our knowledge, the sensitivity of the 1 μm thick devices is the highest reported so far for this thickness, about four times higher than previously reported values for thin-film passive detectors.[64]

Another important figure of merit for ionizing radiation detectors is the limit of detection (LoD), commonly defined as the equivalent dose that generates a signal three times higher than the noise level. Low values of LoD reduces the risk of irradiation exposure for routine X-ray examination, but also allows deep examination and tissue imaging, which are of great importance in medical applications.[65] To determine the LoD, we performed the same irradiation protocol as before (dynamic measurements performed at 0 V bias and with 20 s modulation period) but at lower dose rates, from 2.1 to 81.4 μGy s^{-1} (Figure S12, Supporting Information). Figure 4d shows the extracted photocurrent as a function of dose rates and the respective linear fit. The measured limit of detection was 2.0 ± 1.6 and 11.9 ± 0.6 μG s^{-1} for the two perovskite thicknesses (550 nm and 1 μm), respectively. The thinner perovskite film shows the lowest LoD, a value comparable to the typical dose rates used in medical diagnostic applications (typically >5.5 μGy s^{-1}).[66] The performance of these vacuum deposited thin-film perovskite X-ray detectors is particularly suitable for dosimetry where thin, real-time, radiation transparent, passive electronic detectors could be successfully employed. The current technologies for live monitoring are typically rigid devices and difficult to integrate, like fiber-optic dosimeters.[67] Thus thin-film X-ray detector dosimeter devices based on perovskites can be a desirable alternative.

3. Conclusion

In conclusion, we have developed high-performing p-i-n perovskite photodiodes via optimization of the hole transport layers (HTLs) using vacuum deposition techniques. Several HTL structures have been evaluated, chosen as representative of the most used ones in thin film organic and perovskite diodes. We

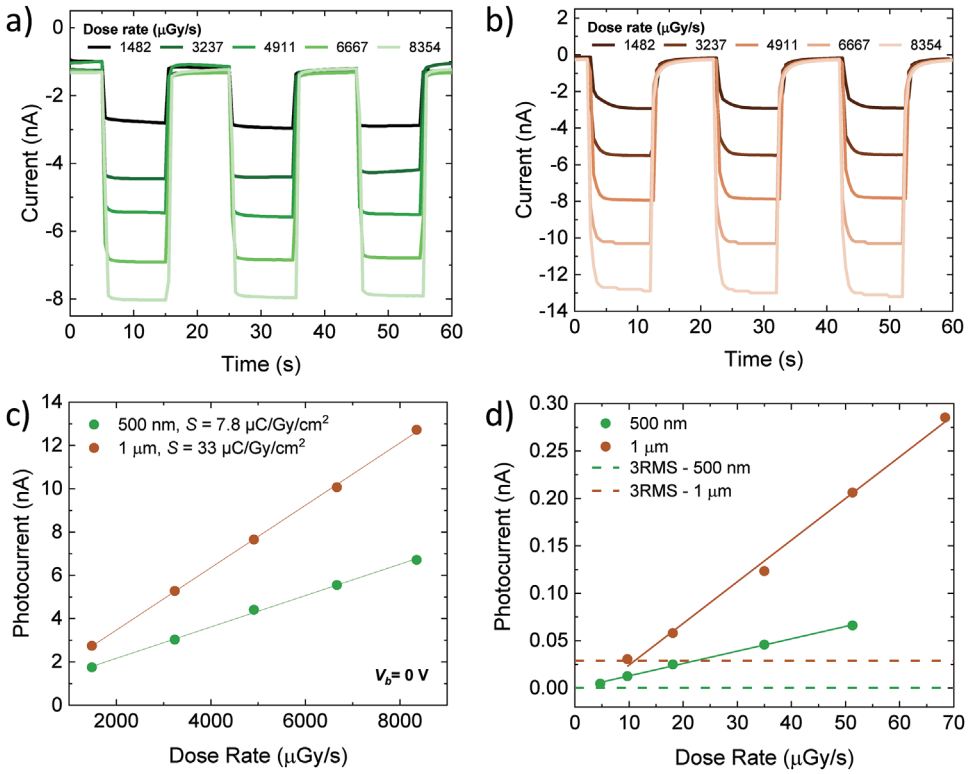

Figure 4. Characterization of the perovskite X-ray detectors. Dynamic response at 0 V bias under various dose rates of X-ray irradiance for the two-perovskite thickness, a) 550 nm and b) 1 μm; and extracted photocurrent of the photodiodes (colored circles) as a function of applied dose rate at 0 V bias for c) high dose rates (from 1482 to 8354 μGy s^{-1}) and d) low dose rates (from 2.13 to 64. μGy s^{-1}).

show that the choice of the vacuum-deposited HTL plays an important role in the performance of the devices, as it directly influences the dark current via thermal charge generation. We obtained low values of noise current down to ≈3 10^{-14} A $Hz^{-1/2}$ with a combination of doped and intrinsic organic semiconductor as HTL, resulting in a high specific detectivity of ≈10^{12} Jones at 710 nm (at −0.5 V reverse bias). The vacuum-deposited perovskite photodiodes were also tested as X-ray detectors. The sensitivity of the detectors was as high as 33 ± 4 μC Gy^{-1} cm^{-2} for a perovskite film thickness of 1 μm. The devices were stable under X-ray radiation and showed a low limit of detection of 2.0 ± 1.6 μG s^{-1} for a thinner (500 nm) perovskite absorber. The 1 μm thick X-ray detectors are among the most sensitive perovskite photodiodes reported so far for similar thicknesses. In general, we show how fully vacuum-processed perovskite photodiodes offer performance on par with state-of-the-art solution-processed devices, both in visible and X-ray sensing, while using techniques more suitable for the industrial environment.

4. Experimental Section

Materials: *N*4,*N*4,*N*4′′,*N*4′′-tetra([1,1′-biphenyl]−4-yl)-[1,1′:4′,1″-terphenyl]−4,4′-diamine (TaTm) was purchased from Tokyo Chemical Industry. Fullerene (C_{60}) was purchased from Merck KGaA. CH_3NH_3I (MAI), PbI_2, MoO_3, bathocuproine (BCP) and CS90112 were purchased from Luminescence Technology Corp. All materials were used as received.

Device Fabrication: Pre-patterned ITO-coated glass substrates were subsequently cleaned with soap, water, and isopropanol in an ultrasonic bath, followed by a 20 min UV–ozone treatment. Substrates were transferred to a vacuum chamber integrated in a nitrogen-filled glovebox and evacuated to a pressure of 10^{-6} mbar. The deposition rate for TaTm and C_{60} was 0.6 Å s^{-1} while the thinner BCP layer was sublimed at 0.2 Å s^{-1}. Ag was deposited in a second vacuum chamber using aluminum boat as source by applying currents ranging from 2.5 to 4.5 A. The deposition rate for the co-deposited doped layers was 0.8 Å s^{-1} for TaTm and 0.08 and 0.12 Å s^{-1} for the dopant (CS90112), achieving TaTm:CS90112 of 9 and 13% wt., respectively. For $MAPbI_3$ deposition, MAI and PbI_2 precursors were simultaneously evaporated following a procedure recently published by the group:[68] in summary, the evaporation chamber employed had only two QCMs, one close to the PbI_2 source designated to monitor exclusively the PbI_2 precursor (PbI_2-QCM), with no cross reading, and a second one fixed at the height of the substrates to monitor simultaneously the total amount of PbI_2 and MAI mass reaching the substrates ($MAPbI_3$-QCM). Initially, only PbI_2 was heated, and the temperature was fine-tuned to lead to a stable sublimation rate of precisely 0.50 Å s^{-1} on both PbI_2-QCM and $MAPbI_3$-QCM. Then, MAI was heated, and the temperature was adjusted so that the sublimation detected on the $MAPbI_3$-QCM increased from the previous 0.50 to 0.66 Å s^{-1}, while the rate on the PbI_2-QCM was kept stable at 0.50 Å s^{-1}.[68] During the evaporation the pressure of the chamber was maintained at 5 × 10^{-6} mbar. For the encapsulation, Al_2O_3 (30 nm) was deposited by atomic layer deposition in a reactor (Arradiance) at 40 °C, using a previously published protocol.[69] A photograph with device layout was shown in Figure S13 (Supporting Information).

Characterization: The *J*–*V* curves under light conditions of the photodiodes were recorded with a Keithley 2612A SourceMeter in a −0.5 and 1.5 V voltage range with 0.01 V steps and were illuminated under a Wavelabs Sinus 70 LED solar simulator using a custom LabVIEW program. The light intensity was calibrated before every measurement using a calibrated Si reference diode. In the EQE measurements the device was illuminated

with a Quartz-Tungsten-Halogen lamp (Newport Apex 2-QTH) through a monochromator (Newport CS130-USB-3-MC), a chopper at 279 Hz and a focusing lens. The device current was measured as a function of energy from 3.5 to 1.5 eV in 0.05 eV steps using a lock-in amplifier (Stanford Research Systems SR830). The system was calibrated, and the solar spectrum mismatch was corrected using a calibrated Si reference cell. The dark *J–V* curves were recorded with a Keithley 6485 Picoammeter in a −0.5 and 1.5 V voltage range with 0.02 V steps applied with a Keithley 2612A SourceMeter. To avoid charging effects and capacitance, dark current density was recorded under applied constant bias voltage over time until a steady-state value was reached. Noise measurements were performed at room temperature and in dark conditions, exploiting a battery-powered current to voltage conversion readout circuit developed with off-the-shelf components. The setup was further arranged in a metal enclosure to shield the device under test from electromagnetic interference. The photodiode was connected by means of two probes and triaxial cables to a trans-impedance amplifier (TIA) implemented with the operation amplifier Analog Devices (ADA4530). An adjustable DC voltage source was applied to the non-inverting terminal of the TIA to modify the biasing of the device. The ultraviolet photoelectron spectroscopy (UPS) measurements were performed in a VG EscaLab II system with a base pressure of 10^{-8} Pa using He–I radiation (21.22 eV) and a bias of −6 V. The X-ray source was a Hamamatsu L12161 Microfocus X-ray tube with W target operated at an accelerating voltage of 150 kVp and with filament currents ranging from 10 to 500 µA. The photocurrent was acquired using a Keithley 2614B precision Source/Measure Unit. During all the irradiation measurements, the sample was kept in nitrogen atmosphere. X-ray pulse duration was of 10s.

Supporting Information

Supporting Information is available from the Wiley Online Library or from the author.

Acknowledgements

M.S. and D.T. acknowledge financial support from the Comunitat Valenciana (CISEJI/2022/43 and CIGE/2021/027, respectively). The authors acknowledge support from the Ministry of Science and Innovation (MCIN) and the Spanish State Research Agency (AEI): grant PRE2019-091181 and PID2022-139910NB-I00. The authors thank the process engineers of Holst Centre's R&D Pilot Line and Marco Fattori from Eindhoven University of Technology for building the noise setup. The authors acknowledge funding from the Ministry of Education, Culture, and Science (Gravity program 024.001.035), Netherlands Organisation for Scientific Research (NWO Spinoza grant), and the European Union's Horizon 2020 research and innovation program under the Photonics Public Private Partnership (www.photonics21.org) with the project PEROXIS under the grant agreement No 871336. C.B. acknowledges the funding by EU – NextGenerationEU with funds made available by the National Recovery and Resilience Plan (NRRP) Mission 4, Component 2, Investment 3.3 (MD 352/2022).

Conflict of Interest

The authors declare no conflict of interest.

Data Availability Statement

The data that support the findings of this study are available from the corresponding author upon reasonable request.

Keywords

hole transport layer, metal halide perovskite, perovskite photodetector, perovskite photodiode, X-ray detector

Received: February 19, 2024
Revised: April 15, 2024
Published online: June 5, 2024

[1] H. Zhang, X. Ji, H. Yao, Q. Fan, B. Yu, J. Li, *Sol. Energy* **2022**, *233*, 421.
[2] A. Fakharuddin, M. K. Gangishetty, M. Abdi-Jalebi, S.-H. Chin, A. R. bin Mohd Yusoff, D. N. Congreve, W. Tress, F. Deschler, M. Vasilopoulou, H. J. Bolink, *Nat. Electron.* **2022**, *5*, 203.
[3] Y. Fu, H. Zhu, J. Chen, M. P. Hautzinger, X. Y. Zhu, S. Jin, *Nat. Rev. Mater.* **2019**, *4*, 169.
[4] V. Adinolfi, W. Peng, G. Walters, O. M. Bakr, E. H. Sargent, *Adv. Mater.* **2018**, *30*, 1700764.
[5] L. M. Herz, *ACS Energy Lett.* **2017**, *2*, 1539.
[6] G. E. Eperon, S. D. Stranks, C. Menelaou, M. B. Johnston, L. M. Herz, H. J. Snaith, *Energy Environ. Sci.* **2014**, *7*, 982.
[7] N. J. Jeon, J. H. Noh, W. S. Yang, Y. C. Kim, S. Ryu, J. Seo, S. Il Seok, *Nature* **2015**, *517*, 476.
[8] M. A. Green, E. D. Dunlop, M. Yoshita, N. Kopidakis, K. Bothe, G. Siefer, X. Hao, *Prog. Photovoltaics Res. Appl.* **2023**, *31*, 651.
[9] H. Ren, J. Chen, Y. Li, J. Tang, *Adv. Sci.* **2021**, *8*, 2002418.
[10] X. Huang, Y. Guo, Y. Liu, *Chem. Commun.* **2021**, *57*, 11429.
[11] F. P. García de Arquer, A. Armin, P. Meredith, E. H. Sargent, *Nat. Rev. Mater.* **2017**, *2*, 16100.
[12] T. Yang, F. Li, R. Zheng, *ACS Appl. Electron. Mater.* **2019**, *1*, 1348.
[13] C. Perumal Veeramalai, S. Feng, X. Zhang, S. V. N. Pammi, V. Pecunia, C. Li, *Photonics Res.* **2021**, *9*, 968.
[14] H. Wang, D. H. Kim, *Chem. Soc. Rev.* **2017**, *46*, 5204.
[15] A. J. J. M. van Breemen, R. Ollearo, S. Shanmugam, B. Peeters, L. C. J. M. Peters, R. L. van de Ketterij, I. Katsouras, H. B. Akkerman, C. H. Frijters, F. Di Giacomo, S. Veenstra, R. Andriessen, R. A. J. Janssen, E. A. Meulenkamp, G. H. Gelinck, *Nat. Electron.* **2021**, *4*, 818.
[16] S. F. Leung, K. T. Ho, P. K. Kung, V. K. S. Hsiao, H. N. Alshareef, Z. L. Wang, J. H. He, *Adv. Mater.* **2018**, *30*, 1704611.
[17] D. Tordera, B. Peeters, H. B. Akkerman, A. J. J. M. van Breemen, J. Maas, S. Shanmugam, A. J. Kronemeijer, G. H. Gelinck, *Adv. Mater. Technol.* **2019**, *4*, 1900651.
[18] A. Rogalski, P. Martyniuk, M. Kopytko, W. Hu, *Appl. Sci.* **2021**, *11*, 501.
[19] A. Moeini, L. Martínez-Sarti, K. P. S. Zanoni, M. Sessolo, D. Tordera, H. J. Bolink, *J. Mater. Chem. C* **2022**, *10*, 13878.
[20] D. Hao, J. Zou, J. Huang, *InfoMat* **2020**, *2*, 139.
[21] Y. Wang, C. Chen, T. Zou, L. Yan, C. Liu, X. Du, S. Zhang, H. Zhou, *Adv. Mater. Technol.* **2020**, *5*, 1900752.
[22] W. Wang, D. Zhao, F. Zhang, L. Li, M. Du, C. Wang, Y. Yu, Q. Huang, M. Zhang, L. Li, J. Miao, Z. Lou, G. Shen, Y. Fang, Y. Yan, *Adv. Funct. Mater.* **2017**, *27*, 1703953.
[23] C. C. Stoumpos, C. D. Malliakas, J. A. Peters, Z. Liu, M. Sebastian, J. Im, T. C. Chasapis, A. C. Wibowo, D. Y. Chung, A. J. Freeman, B. W. Wessels, M. G. Kanatzidis, *Cryst. Growth Des.* **2013**, *13*, 2722.
[24] Y. Zhou, J. Chen, O. M. Bakr, O. F. Mohammed, *ACS Energy Lett.* **2021**, *6*, 739.
[25] H. Wei, J. Huang, *Nat. Commun.* **2019**, *10*, 1066.
[26] Z. Saki, M. M. Byranvand, N. Taghavinia, M. Kedia, M. Saliba, *Energy Environ. Sci.* **2021**, *14*, 5690.
[27] J. Lee, K. Lee, K. Kim, N. G. Park, *Sol. RRL* **2022**, *6*, 2200623.
[28] M. I. Pintor Monroy, I. Goldberg, K. Elkhouly, E. Georgitzikis, L. Clinckemalie, G. Croes, N. Annavarapu, W. Qiu, E. Debroye, Y. Kuang, M. B. J. Roeffaers, J. Hofkens, R. Gehlhaar, J. Genoe, *ACS Appl. Electron. Mater.* **2021**, *3*, 3023.
[29] X. Liu, Z. Liu, J. Li, X. Tan, B. Sun, H. Fang, S. Xi, T. Shi, Z. Tang, G. Liao, *J. Mater. Chem. C* **2020**, *8*, 3337.

[30] N. R. Al Amin, C. C. Lee, Y. C. Huang, C. J. Shih, R. Estrada, S. Biring, M. H. Kuo, C. F. Li, Y. C. Huang, S. W. Liu, *ACS Appl. Mater. Interfaces* **2023**, *15*, 21284.
[31] Z. Zhan, D. Lin, J. Cai, Y. Lu, A. Chen, T. Zhang, K. Chen, P. Liu, X. Wang, W. Xie, *Adv. Mater.* **2022**, *34*, 2207106.
[32] P. T. Lai, H. C. Lin, Y. T. Chuang, C. Y. Chen, W. K. Cheng, G. H. Tan, B. W. Hsu, L. Yang, S. C. Lou, L. J. Chien, H. W. Wang, H. W. Lin, *ACS Appl. Mater. Interfaces* **2022**, *14*, 19795.
[33] W. Li, Y. Xu, J. Peng, R. Li, J. Song, H. Huang, L. Cui, Q. Lin, *ACS Appl. Mater. Interfaces* **2021**, *13*, 2971.
[34] L. Martínez-Goyeneche, L. Gil-Escrig, I. Susic, D. Tordera, H. J. Bolink, M. Sessolo, *Adv. Opt. Mater.* **2022**, *10*, 2201047.
[35] R. Ollearo, J. Wang, M. J. Dyson, C. H. L. Weijtens, M. Fattori, B. T. van Gorkom, A. J. J. M. van Breemen, S. C. J. Meskers, R. A. J. Janssen, G. H. Gelinck, *Nat. Commun.* **2021**, *12*, 7277.
[36] S. Demchyshyn, M. Verdi, L. Basiricò, A. Ciavatti, B. Hailegnaw, D. Cavalcoli, M. C. Scharber, N. S. Sariciftci, M. Kaltenbrunner, B. Fraboni, *Adv. Sci.* **2020**, *7*, 2002586.
[37] L. Gil-Escrig, S. Hu, K. P. S. Zanoni, A. Paliwal, M. A. Hernández-Fenollosa, C. Roldán-Carmona, M. Sessolo, A. Wakamiya, H. J. Bolink, *ACS Mater. Lett.* **2022**, *4*, 2638.
[38] E. Aydin, J. Liu, E. Ugur, R. Azmi, G. T. Harrison, Y. Hou, B. Chen, S. Zhumagali, M. De Bastiani, M. Wang, W. Raja, T. G. Allen, A. U. Rehman, A. S. Subbiah, M. Babics, A. Babayigit, F. H. Isikgor, K. Wang, E. Van Kerschaver, L. Tsetseris, E. H. Sargent, F. Laquai, S. De Wolf, *Energy Environ. Sci.* **2021**, *14*, 4377.
[39] B. Dänekamp, N. Droseros, D. Tsokkou, V. Brehm, P. P. Boix, M. Sessolo, N. Banerji, H. J. Bolink, *J. Mater. Chem. C* **2019**, *7*, 523.
[40] I. Susic, K. P. S. Zanoni, A. Paliwal, I. C. Kaya, Z. Hawash, M. Sessolo, E. Moons, H. J. Bolink, *Sol. RRL* **2022**, *6*, 2100882.
[41] Q. Lin, A. Armin, D. M. Lyons, P. L. Burn, P. Meredith, *Adv. Mater.* **2015**, *27*, 2060.
[42] A. Babaei, K. P. S. Zanoni, L. Gil-Escrig, D. Pérez-del-Rey, P. P. Boix, M. Sessolo, H. J. Bolink, *Front Chem* **2020**, *7*, 936.
[43] D. Pérez-Del-Rey, L. Gil-Escrig, K. P. S. Zanoni, C. Dreessen, M. Sessolo, P. P. Boix, H. J. Bolink, *Chem. Mater.* **2019**, *31*, 6945.
[44] M. Piot, J. Enrique, S. Alonso, K. P. S. Zanoni, N. Rodkey, F. Ventosinos, C. Rold, M. Sessolo, H. Bolink, *ACS Energy Lett.* **2023**, *8*, 4711.
[45] C. Momblona, L. Gil-Escrig, E. Bandiello, E. M. Hutter, M. Sessolo, K. Lederer, J. Blochwitz-Nimoth, H. J. Bolink, *Energy Environ. Sci.* **2016**, *9*, 3456.
[46] J. Avila, L. Gil-Escrig, P. P. Boix, M. Sessolo, S. Albrecht, H. J. Bolink, *Sustainable Energy Fuels* **2018**, *2*, 2429.
[47] R. Ollearo, A. Caiazzo, J. Li, M. Fattori, A. J. J. M. van Breemen, M. M. Wienk, G. H. Gelinck, R. A. J. Janssen, *Adv. Mater.* **2022**, *34*, 2205261.
[48] Q. Lin, A. Armin, R. C. R. Nagiri, P. L. Burn, P. Meredith, *Nat. Photonics* **2015**, *9*, 106.
[49] Y. Fu, Q. Song, T. Lin, Y. Wang, X. Sun, Z. Su, B. Chu, F. Jin, H. Zhao, W. Li, C. S. Lee, *Org. Electron.* **2017**, *51*, 200.
[50] J. Yu, X. Chen, Y. Wang, H. Zhou, M. Xue, Y. Xu, Z. Li, C. Ye, J. Zhang, P. A. Van Aken, P. D. Lund, H. Wang, *J. Mater. Chem. C* **2016**, *4*, 7302.
[51] V. O. Eze, G. R. Adams, L. Braga Carani, R. J. Simpson, O. I. Okoli, *J. Phys. Chem. C* **2020**, *124*, 20643.
[52] D. Liu, B. B. Yu, M. Liao, Z. Jin, L. Zhou, X. Zhang, F. Wang, H. He, T. Gatti, Z. He, *ACS Appl. Mater. Interfaces* **2020**, *12*, 30530.
[53] C. Liu, K. Wang, C. Yi, X. Shi, P. Du, A. W. Smith, A. Karim, X. Gong, *J. Mater. Chem. C* **2015**, *3*, 6600.
[54] S. Xing, J. Kublitski, C. Hänisch, L. C. Winkler, T. yi Li, H. Kleemann, J. Benduhn, K. Leo, *Adv. Sci.* **2022**, *9*, 13.
[55] Y. Fang, A. Armin, P. Meredith, J. Huang, *Nat. Photonics* **2019**, *13*, 1.
[56] F. Furlan, D. Nodari, E. Palladino, E. Angela, L. Mohan, J. Briscoe, M. J. Fuchter, T. J. Macdonald, G. Grancini, M. A. McLachlan, N. Gasparini, *Adv. Opt. Mater.* **2022**, *10*, 2201816.
[57] B. R. Sutherland, A. K. Johnston, A. H. Ip, J. Xu, V. Adinolfi, P. Kanjanaboos, E. H. Sargent, *ACS Photonics* **2015**, *2*, 1117.
[58] A. Mirzehmet, T. Ohtsuka, S. A. Syed, T. Yuyama, P. Krüger, H. Yoshida, *Adv. Mater.* **2021**, *33*, 2004981.
[59] L. Basiricò, A. Ciavatti, B. Fraboni, *Adv. Mater. Technol.* **2021**, *6*, 2000475.
[60] X. Xu, W. Qian, S. Xiao, J. Wang, S. Zheng, S. Yang, *EcoMat* **2020**, *2*, 12064.
[61] K. Sakhatskyi, B. Turedi, G. J. Matt, E. Wu, A. Sakhatska, V. Bartosh, M. N. Lintangpradipto, R. Naphade, I. Shorubalko, O. F. Mohammed, S. Yakunin, O. M. Bakr, M. V. Kovalenko, *Nat. Photonics* **2023**, *17*, 510.
[62] S. Yakunin, M. Sytnyk, D. Kriegner, S. Shrestha, M. Richter, G. J. Matt, H. Azimi, C. J. Brabec, J. Stangl, M. V. Kovalenko, W. Heiss, *Nat. Photonics* **2015**, *9*, 444.
[63] L. Basiricò, S. P. Senanayak, A. Ciavatti, M. Abdi-Jalebi, B. Fraboni, H. Sirringhaus, *Adv. Funct. Mater.* **2019**, *29*, 1902346.
[64] M. Verdi, A. Giuri, A. Ciavatti, A. Rizzo, C. Esposito Corcione, L. Basiricò, S. Colella, B. Fraboni, *Adv. Mater. Interfaces* **2023**, *10*, 2300044.
[65] X. Zhang, S. Yu, X. Meng, S. Xiao, *Cryst. Res. Technol.* **2023**, *58*, 2200232.
[66] I. Clairand, J. M. Bordy, E. Carinou, J. Daures, J. Debroas, M. Denozire, L. Donadille, M. Ginjaume, C. Itié, C. Koukorava, S. Krim, A. L. Lebacq, P. Martin, L. Struelens, M. Sans-Merce, F. Vanhavere, *Radiat. Meas.* **2011**, *46*, 1252.
[67] S. Beddar, L. Beaulieu, *Scintillation Dosimetry*, (Eds: S. Beddar, L. Beaulieu), 1st ed., CRC Press, Boca Raton **2016**.
[68] K. P. S. Zanoni, L. Martínez-Goyeneche, C. Dreessen, M. Sessolo, H. J. Bolink, *Sol. RRL* **2023**, *7*, 2201073.
[69] I. C. Kaya, K. P. S. Zanoni, F. Palazon, M. Sessolo, H. Akyildiz, S. Sonmezoglu, H. J. Bolink, *Adv. Energy Sustainable Res.* **2021**, *2*, 2000065.